

Self induced Hall Effect in current carrying bar

M. V. Cheremisin

A.F.Ioffe Physical-Technical Institute, St.Petersburg, Russia

(Dated: June 16, 2023)

The longitudinal current in a three-dimensional conductor is accompanied by transverse magnetic field in a specimen bulk. The absence of the transverse current in a sample bulk requires a nonzero Hall electric field in transverse cross-section which provides the Lorentz force cancellation. The longitudinal current itself can be viewed as a collective drift of carriers in crossed magnetic and electric(Hall) fields. At low temperatures the enhanced carrier viscosity leads to nonuniform current flow whose transverse profile is sensitive to presence of *collinear* diamagnetic currents at the sample inner walls. Former dissipative the longitudinal current becomes purely diamagnetic at certain critical temperature. The superconductivity sets on. The current and transverse magnetic field become pushed out from the sample bulk towards the inner wall. Magnetic properties of a sample resemble those expected for ideal diamagnet. The threshold of superconductivity is calculated for arbitrary temperature, disorder strength, sample size and current and(or) magnetic field strength. Sample-size and magnetic field driven transition from normal metal phase to superconductivity has been studied. The superconductivity phase is not discussed.

I. INTRODUCTION

Usually, the Hall measurements¹ imply a presence of external magnetic field affecting the carrier transport. The typical scheme of the Hall bar geometry sample is shown in Fig.1. Evidence shows that the current itself may produce a finite magnetic field which, in turn, influences the current carrying state. In present paper, we take the interest in a special case of the magnetic field induced by the current itself. We reveal a self-consistent Hall Effect. Taking into account finite carrier viscosity and diamagnetic currents persistent at inner sample walls we demonstrate feasibility of the superconductivity at low temperatures.

II. CURRENT INDUCED HALL EFFECT IN A BAR SAMPLE

The conventional Drude equation for electron gas in presence of arbitrary electric \mathbf{E} and magnetic \mathbf{B} fields yields

$$\frac{\partial \mathbf{V}}{\partial t} = \frac{e\mathbf{E}}{m} + [\mathbf{V} \times \boldsymbol{\Omega}_c] - \frac{\mathbf{V}}{\tau}, \quad (1)$$

where \mathbf{V} is the electron flux velocity, e is the absolute value of the electronic charge. Then, $\boldsymbol{\Omega}_c = \frac{e\mathbf{B}}{mc}$ is a vector whose absolute value corresponds to local cyclotron frequency, m is the effective mass, τ is the momentum relaxation time due to collisions with impurities and(or) phonons.

For steady state Eq.(1) yields

$$\mathbf{V} = \mu\mathbf{E} + [\mathbf{V} \times \boldsymbol{\Omega}_c\tau], \quad (2)$$

where $\mu = \frac{e\tau}{m}$ is the carrier mobility. For arbitrary orientation of the electric and the magnetic fields the exact solution of Eq.(2) is straightforward².

We further restrict ourself to a certain sample geometry, namely consider the bar sample of thickness d which is less than both the width w and the length L . Let a voltage source(not shown in Fig.1) is attached to sample contacts providing the longitudinal electric field E_z in a sample bulk. Evidence shows that longitudinal carrier velocity V_z and, hence,

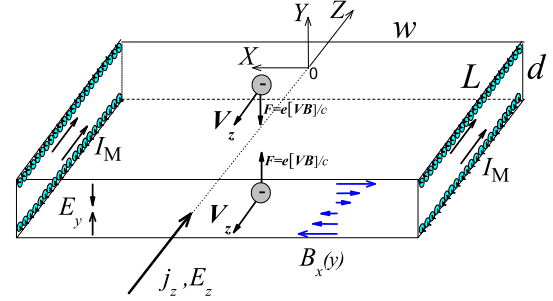


FIG. 1: Schematic view of the self-consistent Hall effect. The Lorentz force is shown for electron moved in top(bottom) half-space of the sample bulk. The average diamagnetic currents I_M caused by microscopic cyclotron movement of electrons in the vicinity of the top(bottom) inner wall are shown.

the respective current density $j_z = neV_z$ are uniform for constant electron density n . One may easily find x-component of the transverse magnetic field $B_x(Y) = -\frac{4\pi j_z}{c}Y$ followed from Biot-Savart law. Notably, the transverse magnetic field reaches its maximal value $B_0 = \frac{2\pi I}{cw}$ at the top(bottom) wall of the slab, where $I = j_z dw$ is the total current. Evidence shows that the transverse components of the current density are absent in a sample bulk, i.e $j_{x,y} \equiv 0$. Hence, in presence of the transverse magnetic field B_x a nonzero y-component of the electric field E_y must exist to prevent Lorentz force plays $\sim V_z B_x/c$ Evidently, the build-in transverse field E_y plays a role of the Hall electric field in conventional description¹.

Following the above reasoning we re-write Eq.(2) for both the longitudinal V_z and transverse $V_y = 0$ components of the

carrier velocity:

$$V_z = \mu E_z, \quad (3)$$

$$V_z = c \frac{E_y}{B_x}. \quad (4)$$

Eq.(3) represents a familiar description of differential Ohm's law $j_z = j_D$, where $j_D = ne\mu E_z$ is the Drude current. By contrast, Eq.(4) presents the novel view on the longitudinal current as a drift of carriers in crossed $E_y \perp B_x$ fields, i.e. ascribes self-consistent Hall Effect. We argue that the build-in electric field $E_y = 4\pi neY \left(\frac{V_z}{c}\right)^2$ defines volumetric charge density $Q = \text{div}\mathbf{E}/4\pi = ne \left(\frac{V_z}{c}\right)^{2,4}$. Thus, a sample bulk is charged, i.e. $Q/ne \ll 1$.

III. HALL EFFECT: NONUNIFORM VISCOUS FLOW

We now intend to answer a question whether the current carrying state in a bar could be nonuniform in transverse direction, namely we presume $V_z(Y)$. To resolve the problem, we will use Navier-Stokes equation valid for viscous electron fluid

$$\frac{\partial \mathbf{V}}{\partial t} + (\mathbf{V} \nabla) \mathbf{V} = \frac{e\mathbf{E}}{m} + [\mathbf{V} \times \boldsymbol{\Omega}_c] + \hat{\eta} \Delta \mathbf{V} - \frac{\mathbf{V}}{\tau} \quad (5)$$

in presence of the magnetic field. Here, $\hat{\eta}$ is the viscosity tensor⁵ whose longitudinal and transverse components

$$\begin{aligned} \eta_{xx} = \eta_{yy} &= \frac{\eta}{1 + 4\Omega_c^2 \tau_\eta^2}, \\ \eta_{xy} &= -\eta_{yx} = \eta_{xx} 2\Omega_c \tau_\eta \end{aligned} \quad (6)$$

depend on magnetic field. Then, $\eta = \frac{1}{5} V_F^2 \tau_\eta$ is the kinematic viscosity of the carriers at zero magnetic field, V_F is the Fermi velocity, τ_η denotes viscosity relaxation time whose exact form will be specified further. Viscosity effects start to be important^{6,7} when the mean free path $l_\eta = V_F \tau_\eta$ becomes less and(or) comparable to that $l = V_F \tau$ caused by phonons and(or) impurities and typical length scale of the sample.

One may easily check that for present case of nonuniform flow the Euler term in a left part of Eq.(5) is equal to zero. Therefore, for steady state Eq.(5) can be re-written for both the longitudinal and transverse direction as it follows

$$\eta_{xx} \tau \frac{\partial^2 V_z}{\partial^2 Y} - V_z + \mu E_z = 0, \quad (7)$$

$$\eta_{yx} \frac{\partial^2 V_z}{\partial^2 Y} + \frac{eE_y}{m} - \frac{V_z e B_x}{mc} = 0. \quad (8)$$

Our primary interest concerns Eq.(7) which determines the nonuniform velocity profile $V_z(Y)$ and, in turn, the transverse magnetic field $B_x(Y)$

$$B_x = -\frac{2\pi ne}{c} \int_{-Y}^Y V_z(Y) dY. \quad (9)$$

Introducing the dimensionless velocity $v = V_z/\mu E_z$ and the reduced transverse co-ordinate $y = Y/d$, one may rewrite Eq.(7) as it follows

$$\frac{\eta_{xx}}{\eta} \nu^{-2} \frac{\partial^2 v}{\partial^2 y} - v + 1 = 0. \quad (10)$$

where $\nu = d/\lambda$ is the dimensionless parameter. Then, $\lambda = \sqrt{\eta\tau}$ denotes the typical length scale of velocity profile $v_z(y)$ sharpness. The condition $\nu \ll 1$ ($\nu \gg 1$) determines the high(low)-viscous electron gas respectively.

We argue that solving of Eq.(10) is complicated because of field dependent viscosity pre-factor $\eta_{xx}(\Omega_c) \rightarrow \eta_{xx}(y)$ in the highest derivative term. In principle, Eq.(10) can be expressed in terms of the reduced magnetic field $B_x(y)/B_0$ via relationship $v = \frac{1}{2B_0} \frac{dB_x}{dy}$ but still remains difficult for analytic analysis. However, we may restrict ourself to low-current and(or) small magnetic field case when $\Omega_c \tau_\eta \ll 1$. By doing so, the longitudinal viscosity can be kept constant $\eta_{xx} \sim \eta$. The solution of Eq.(7) becomes straightforward:

$$v(y) = 1 + C_1 \cosh(\nu y) + C_2 \sinh(\nu y), \quad (11)$$

The actual geometry of the problem yields the symmetric condition $v|_{y=\pm 1/2} = v_0$ for longitudinal velocity at the inner bar walls. Therefore, we obtain

$$v(y) = 1 + (v_0 - 1) \frac{\cosh(\nu y)}{\cosh(\nu/2)}, \quad (12)$$

The Drude uniform flow follows from Eq.(12) when $v = v_0 = 1$ and was examined in Sec.II already. For arbitrary condition $v_0 \neq 1$ at the inner bar walls the profile of longitudinal velocity is expected to be affected crucially by viscosity effects. The primary goal of the present paper concerns the calculation of the sample resistivity affected by boundary conditions and viscosity strength.

A final note concerns Eq.(8) which gives previous result specified by Eq.(4) for carrier drift in crossed $E_y \perp B_x$ fields when $\eta_{xy} \rightarrow 0$.

A. Poiseuille viscous flow

Let us first consider a simple case of wall adhesion condition $v_0 = 0$ ⁶ followed from analysis of Poiseuille's viscous flow known in conventional hydrodynamics. In Fig.3 the blue curves depict the spatial dependence of the flux velocity $v(y)$ specified by Eq.(12) for different viscosity strengths. As expected, for small viscosity $\nu \gg 1$ the fluid velocity is mostly uniform excepting ultra-narrow layer $\sim \lambda$ close to bar inner walls. In contrast, for highly viscous case $\nu \leq 1$ the flux velocity follows the Poiseuille's flow law $v(y) = \frac{\nu^2}{2} (\frac{1}{4} - y^2)$ shown by the dashed line in Fig.3.

B. Diamagnetic viscous flow

The special interest of the present paper concerns a possibility of unusual boundary condition $v_0 > 1$ whose physical background will be illustrated hereafter.

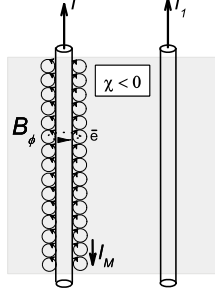


FIG. 2: The macroscopic magnetic current I_M for current carrying conductors placed into diamagnetic $\chi < 0$ media (under Ref.⁹).

At first, recall a scenario of a current carrying wire surrounded by diamagnetic media shown in Fig.2. The current I is provided by external source. We assume the diamagnetic susceptibility $\chi < 0$ of the environment caused, for clarity, by the electrons orbital movement⁸. The current carrying wire induces the azimuthal magnetic field $B_\varphi = \frac{2I}{cR}$ in the surrounding space $R > R_0$. Notably, the magnetic field at the outer wire wall B_0 results in negative macroscopic current $I_M = 4\pi\chi I^{9,10}$ because of diamagnetic environment. The total current flowing along the wire $I + I_M < I$. Let an another conductor with a co-directional current $I_1 \parallel I$ (see Fig.2,a) is placed in parallel to the initial one. Again, the total current along the second wire $(1 + 4\pi\chi)I_1$ includes the negative component $4\pi\chi I_1$ (not shown in Fig. 2,a) as well. One can check that Ampere's attractive force $\sim (1 + 4\pi\chi)I \cdot I_1$ between the pair of wires with parallel currents is reduced by a factor of $1 + 4\pi\chi^9$ compared to that in absence of diamagnetic environment. Evidently, the Ampere's force diminution is caused by microscopic magnetic currents at the outer wire surface.

We now provide a strong evidence of similar effect for current carrying bar sample(see Fig.1) which exhibits diamagnetic susceptibility $\chi < 0$ itself. Indeed, for certain applied current I the transverse magnetic field at internal walls of the slab $B_x(\pm d/2) = \mp B_0$ results in the extra diamagnetic current I_M which, in turn, is *collinear* to native current, namely $I_M = 4\pi|\chi|I$. Phenomenologically, one may imagine a diamagnetic current which flows within narrow layers of a width δ in the vicinity of up(down) sample walls. The respective diamagnetic current density $j_M = \frac{I_M}{2\delta w}$ becomes proportional to transverse magnetic field B_0 at the sample walls:

$$j_M = \frac{|\chi|cB_0}{\delta} \quad (13)$$

and could, in principle, exceed the Drude current density j_D .

One may write down the dimensionless flux velocity v_0 at the inner rod surface as

$$v_0 = \frac{j_M}{j_D} = \frac{\bar{j}}{j_D} \kappa, \quad (14)$$

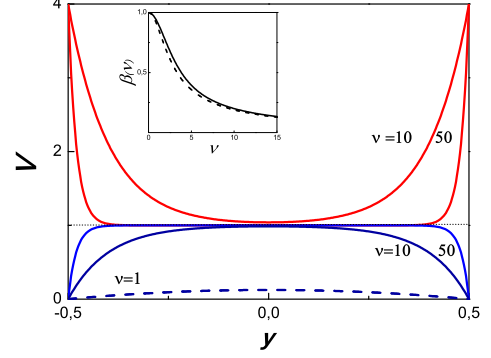


FIG. 3: Flux velocity distribution $v(y)$ specified by Eq.(12) at fixed applied longitudinal electric field and viscosity parameter $\nu = 10; 50$ for wall adhesion boundary condition $v_0 = 0$ (blue) and diamagnetic boundary condition $v_0 = 4$ (red). The Poiseuille flow for $v_0 = 0; \nu = 1$ is shown by the dashed line. Dotted line represents uniform flow $v = v_0 = 1$. Inset: universal dependence $\beta(\nu)$ for bar(wire) is shown by solid(dashed) line respectively.

where $\bar{j} = \frac{I}{dw}$ is the average current density. Then, we introduce the dimensionless parameter

$$\kappa = \frac{2\pi d|\chi|}{\delta}, \quad (15)$$

which depends on the sample size. Without diamagnetic currents, i.e. when $\kappa = 0$, we recover the Poiseuille's flow when the wall-adhesion condition $v_0 = 0$ remains valid.

Our major interest concerns the strong diamagnetic case when $\kappa \geq 1$. In Fig.3 we plot the transverse distribution $v(y)$ at fixed boundary velocity $v_0 = 4$ and different viscosity strengths. As expected, the diamagnetic current within a narrow layer δ initiates a current flow within a wider stripe $\lambda \gg \delta$ close to sample inner wall. The flux velocity approaches the Drude value in a sample bulk, i.e. when $v = 1$. Using Eq.(12)

we find out the average current density $\bar{j} = \frac{ne}{d} \int_{-d/2}^{d/2} V_z(Y) dY$ as it follows

$$\bar{j} = j_D [1 + (v_0 - 1)\beta(\nu)], \quad (16)$$

where $\beta(\nu) = \frac{2}{\nu} \tanh(\frac{\nu}{2})$ is the universal function(see Fig.3,inset) of the viscosity strength. The function $0 < \beta(\nu) \leq 1$ decreases smoothly as $\sim 1 - \nu^2/12$ for high-viscous case $\nu \ll 1$ and, then follows the asymptote $\sim 2/\nu$ for low viscosities $\nu \gg 1$.

Remarkably, the all previous reasoning are valid for a wire whose radius plays the role of the sample thickness d in present notations. For wire the universal function $\beta(\nu)$ in present notations. For wire the universal function $\beta(\nu)$ embedded into Eq.(16) can be replaced by $\beta_{wire}(\nu) = \frac{2J_1(\nu)}{\nu J_0(\nu)}$, where $J_{0(1)}$ is the zero(first)-order modified Bessel function of the first kind. The dependence $\beta_{wire}(\nu)$ is shown by the dashed line in Fig.3,inset. Both dependencies are close one to each other, therefore our forthcoming discussion could be similar for wire case as well.

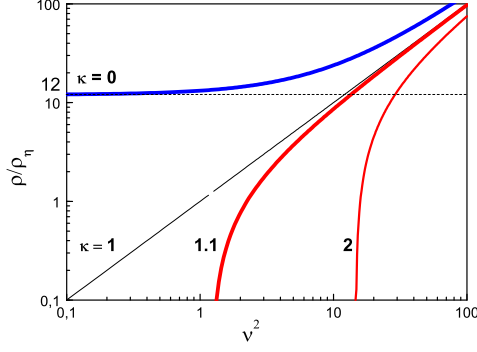


FIG. 4: Dimensionless resistivity ρ/ρ_η followed from Eq.(18) vs dimensionless disorder strength $\nu^2 = \frac{d^2}{\eta\tau}$ for: zero diamagnetic current $\kappa = 0$; uniform current state $\kappa = 1$; strong diamagnetism $\kappa > 1$. Dashed line represents the viscous resistivity $\rho = 12\rho_\eta$ at $\kappa = 0$ and $1/\tau \rightarrow 0$.

Using Eq.(14) the self-consistent solution of Eq.(16) reads

$$\bar{j} = j_D \frac{1 - \beta}{1 - \kappa\beta}. \quad (17)$$

Noticeably, Eq.(17) defines the average current density at fixed longitudinal electric field E_z . Consequently, one may define the "effective resistivity" $\rho = \frac{E_z}{\bar{j}}$ as it follows

$$\rho = \rho_D \frac{1 - \kappa\beta}{1 - \beta}. \quad (18)$$

Here, $\rho_D = \frac{m}{ne^2\tau}$ is the conventional Drude resistivity, $\mu_D = (ne\rho_D)^{-1}$ is the mobility.

Eq.(18) represents the central result of the paper. The galvanic measurements provide the "effective resistivity" which differs with respect to Drude value. Namely, the "effective resistivity" depends on the size and, moreover, the diamagnetic properties of the sample. At first, for $\kappa = 1$ one recovers the Drude uniform current flow without viscous effects included, hence $\rho = \rho_D$. Secondly, the wall adhesion condition $\kappa = 0$ provides the "effective resistivity" in a Gurzhi form $\rho = \rho_D/(1 - \beta)$ reported in Ref.⁶. For low-viscosity case $\nu \gg 1$ the "effective resistivity" is still described by Drude formulae $\rho \sim \rho_D$. In the opposite high-viscosity and/or low dissipation limit $\nu \ll 1$ the Poiseuille type of a current flow is realized. The "effective resistivity" at $\nu \ll 1$ is given by the asymptote $\rho = 12\rho_\eta$, where $\rho_\eta = \frac{m}{ne^2} \frac{\eta}{d^2}$ is so-called "viscous" resistivity⁶ which depends on the sample size. Note, the ratio d^2/η plays the role of the momentum relaxation time similar to that discussed^{11,12} for 2D electron gas. The transition from Drude to "viscous" resistivity case occurs at $\nu \sim 1$. In Fig.4 we plot the reduced resistivity ρ/ρ_η vs disorder $\nu^2 \sim 1/\tau$ for fixed viscosity strength η and different values of diamagnetic parameter κ . Noticeably, for arbitrary value of the diamagnetic parameter κ the resistivity in Fig.4 starts to follow conventional Drude dependence for high disorder and/or low viscosity $\nu \gg 1$.

The most intriguing result followed from Eq.(18) concerns the strong diamagnetism case $\kappa > 1$ when the effective resistivity vanishes at

$$\kappa \cdot \beta(\nu) = 1. \quad (19)$$

Eq.(19) gives the critical condition for zero resistivity, i.e. the superconductivity¹⁴. Recall that for arbitrary argument $\beta(\nu) \leq 1$. Hence, the superconductivity would appear when the condition $\kappa > 1$ is satisfied. The latter can be re-written in terms of film size as $d \geq d_m$, where we make use of minimal sample thickness

$$d_m = \frac{\delta}{2\pi|\chi|}, \quad (20)$$

for which the superconductivity can be realized. We further demonstrate that superconductivity criteria $\kappa = d/d_m > 1$ is even stronger for real systems.

We emphasize that the superconductivity may appear for even finite momentum relaxation time. This result looks like mysterious at a first glance. Nevertheless, the experimental data¹⁵ provide a strong evidence of the disorder remains finite whenever the superconductivity is present. A finite momentum relaxation time was estimated¹⁵ for lead as $T \rightarrow 0$.

The actual physics of superconductivity is rather transparent. The non-dissipative diamagnetic current is pinched within a narrow inner layer $\lambda \sim d_m/2$ of a slab and, hence shunts the dissipative Drude flow in the sample bulk. The total current in a sample becomes purely diamagnetic when Eq.(19) is fulfilled.

C. Size effect of superconductivity transition

We now examine in greater details the critical condition given by Eq.(19). One can find, in principle, the critical dependence in a form $\nu^{cr}(\kappa)$. The latter is, however, non-informative since both variables κ, ν depend on the sample size. To avoid this problem, let us introduce a size-free parameter $z = \frac{\nu}{2\kappa} = \frac{d_m}{2\lambda}$. With the help of the above notation the modified Eq.(19) yields

$$\kappa = \frac{\text{arctanh}(z)}{z} \quad (21)$$

and denotes the desired critical diagram in a compact form since $z^{cr}(\kappa) < 1$. The latter is shown in Fig.5,a. The area below the critical curve corresponds to superconductivity. For sample thickness closed to its minimal value d_m , i.e. when $\kappa - 1 \ll 1$, the critical curve follows the asymptote $z = \sqrt{3(\kappa - 1)}$ depicted by the dashed line in Fig.5,a. Then, the critical curve saturates asymptotically as $\kappa = \ln(\frac{2}{1-z})/(2z)$ for bulky sample, i.e. when $\kappa \gg 1$.

We now find superconductivity threshold in terms of temperature by looking at parameter $z \sim 1/\lambda = 1/\sqrt{\eta\tau}$. Remind that for actual low-temperature case the transport is governed mostly by scattering on static defects, hence one may consider a constant momentum relaxation time $\tau \neq \tau(T)$. A point of interest is the scattering time τ_η embedded into components of

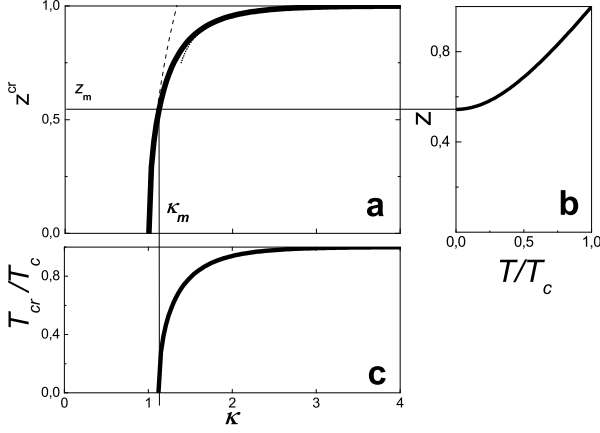


FIG. 5: a) The critical diagram $z^{\text{cr}}(\kappa)$ of superconductivity followed from Eq.(21). The asymptotes for small $\kappa - 1 \ll 1$ and bulky sample $\kappa \gg 1$ are shown by dashed and dotted line respectively. The area below the critical curve $z^{\text{cr}}(\kappa)$ corresponds to superconductivity. b) The dependence $z(\Theta)$ specified by Eq.(29); c) Temperature threshold $\Theta_{\text{cr}}(\kappa)$ specified by Eq.(30) for fixed $z_m = 0.54$.

viscosity tensor specified by Eq.(6). A common belief is that the carrier viscosity is caused solely by e-e collisions with the reciprocal scattering time¹⁶⁻¹⁸

$$\frac{1}{\tau_{ee}(\xi)} = \frac{\xi^2}{\tau_1} \quad (22)$$

dependent on the reduced temperature $\xi = T/T_F$. Here, $T_F = \varepsilon_F/k$ and ε_F are the Fermi temperature and energy respectively. Then, $\tau_1 = l_1/V_F \sim \hbar/\varepsilon_F$ ¹⁷ is the path time of interelectronic distance $l_1 \sim n^{-1/3}$. At low temperatures the e-e collisions becomes strongly dumped because of Pauli principle, therefore the e-e mean free path $l_{ee} = \tau_{ee}V_F$ becomes infinite. Consequently, one expects an infinite electron viscosity. The whole story is that apart from e-e scattering contribution any process yielding the relaxation of the second moment of the electron distribution function (for example, the scattering on static defects) would influence^{5,12} the electron viscosity. With the aid of standard Mattis's rule, one may write down the reciprocal viscosity length as it follows

$$\frac{1}{l_\eta} = \frac{\xi^2}{l_1} + \frac{1}{l_0}, \quad (23)$$

where l_0 defines the residual value at $T \rightarrow 0$. The hydrodynamic approach is valid when $l_\eta \leq l$. Further, we will use recent argumentation¹³ and verify the above criterion for actual case of dirty metals.

With the help of Eq.(23) the variable $z = \frac{d_m}{2\lambda}$ becomes temperature dependent, namely

$$z(\xi) = z_m \sqrt{1 + \gamma \xi^2}, \quad (24)$$

where $z(0) = z_m = \frac{\sqrt{5}d_m}{2\sqrt{l_0l}}$ is the zero-temperature value, $\gamma = l_0/l_1$ is the dimensionless ratio. Recall that threshold

diagram in Fig.5a demonstrates $z^{\text{cr}}(\kappa) \leq 1$. Hence, the condition $z_m \leq 1$ must be satisfied for superconductivity to be feasible. We re-write this criteria in terms of the carrier mobility as it follows

$$\mu \geq \mu_{\min}, \quad (25)$$

where $\mu_{\min} = \frac{5}{8} \frac{ed_m^2}{\varepsilon_F T_0}$ plays the role of the minimal mobility for which superconductivity is possible. Further, we will use obvious relationship

$$z_m = \sqrt{\mu_{\min}/\mu} \quad (26)$$

as well.

If $z_m < 1$, the only upper part of the threshold diagram in Fig.5,a remains useful, i.e. when $z^{\text{cr}}(\kappa) > z_m$. Then, the equality $z_m = z^{\text{cr}}(\kappa_m)$ denotes a certain value of minimal sample size parameter κ_m , which corresponds to superconductivity threshold at $T = 0$. Evidence shows that at finite temperature the superconductivity can be realized for samples whose sizes satisfy the condition $\kappa \geq \kappa_m$. The latter gives the strict criteria for minimal sample size

$$d \geq d_m \cdot \kappa_m \quad (27)$$

instead of that $d \geq d_m$ discussed earlier.

We now attempt to find out threshold temperature for the most important case of massive sample $\kappa \gg 1$ known to be a universal quantity¹⁴. Indeed, substituting the condition $z(\xi) = 1$ valid for massive sample into Eq.(24) we find out the sought-for threshold temperature

$$T_c = T_F [(\mu/\mu_{\min} - 1)/\gamma]^{1/2}. \quad (28)$$

For clarity, we will label hereafter the all quantities related to superconductivity threshold for bulky sample by index "c". According to Eq.(28), the superconductivity is possible for massive specimen when $\mu \geq \mu_{\min}$. The better the sample quality the higher the threshold temperature.

We emphasize that for finite size sample the threshold temperature is always less than that for bulky samples. Experimentally, the drop in threshold temperature for smaller samples was first reported in Refs.^{19,20}. It is instructive to use the dimensionless temperature $\Theta = T/T_c$ scaled with respect to threshold temperature of bulky sample. Hence, the modified Eq.(24) yields

$$z(\Theta) = \sqrt{z_m^2 + (1 - z_m^2)\Theta^2}, \quad (29)$$

In Fig.5,b we plot the dependence given by Eq.(29). Combining the dependencies $z(\Theta)$ and $z^{\text{cr}}(\kappa)$ specified by Eq.(29) and Eq.(21) respectively we obtain the reduced threshold temperature $\Theta_{\text{cr}} = T_{\text{cr}}/T_c$ as a function of the sample size

$$\Theta_{\text{cr}}(\kappa) = \left[\frac{z^{\text{cr}}(\kappa)^2 - z_m^2}{1 - z_m^2} \right]^{1/2}. \quad (30)$$

Fig.5,c demonstrates an example of threshold dependence given by Eq.(30). As expected, $T_{\text{cr}} = T_c$ for massive sample.

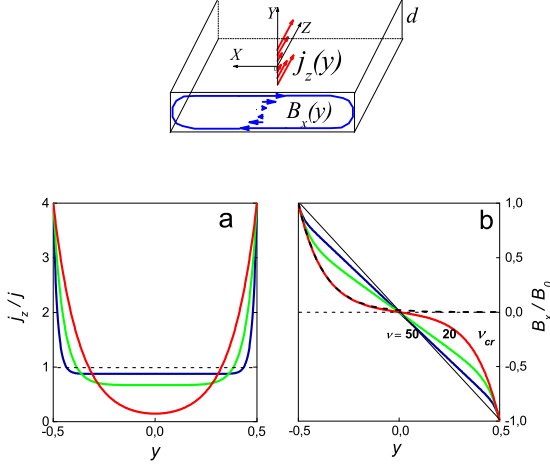


FIG. 6: Top panel: Experimental setup. Dimensionless current density j_z/j_M (panel a) and azimuthal magnetic field B_x/B_0 (panel b) specified by Eq.(31) for finite size sample at $\kappa = 4$ (corresponds to $z^{cr} = 0.999$ and $\nu_{cr} = 2\kappa z^{cr} \cong 8$) and viscosity parameter 8; 20; 50. Thin lines depict the uniform current density case when $\kappa = 1$. Dotted line (insert) corresponds to magnetic field screening asymptote described in text.

D. Magnetic field screening

We now find both the current density and magnetic field spatial profiles for system closer to superconductivity threshold. Recall that the all previous discussion concerned the presence of a finite electric field E_z . Aiming to account for superconductivity (i.e. when $E_z = 0$) we inverse Eq.(17) and, then find the electric field as a function of the average current density \bar{j} . Combining the result with Eq.(12) we obtain the flux velocity distribution in terms of the average current density. The current density profile $j_z(y)$ and transverse magnetic field $B_x(y)$ specified by Eq.(9) read:

$$j_z(y) = \bar{j} \left[\frac{1 - \kappa\beta}{1 - \beta} - \frac{1 - \kappa}{1 - \beta} \cdot \frac{\cosh(\nu y)}{\cosh(\nu/2)} \right], \quad (31)$$

$$B_x(y) = B_0 \left[-2 \frac{1 - \kappa\beta}{1 - \beta} y + \beta \cdot \frac{1 - \kappa}{1 - \beta} \cdot \frac{\sinh(\nu y)}{\sinh(\nu/2)} \right].$$

Eq.(31) gives the correct values of the diamagnetic current density j_M and the amplitude of the magnetic field $B_0 = \frac{2\pi}{c} \bar{j} d$ at the inner walls of the sample $y = \pm 1/2$. For $\kappa = 1$ one recovers the result for uniform current flow, namely $j_z(y) = \bar{j}$, $B_x = -2B_0 y$. As an example, the dependencies given by Eqs.(31) are plotted in Fig.6 for fixed diamagnetic parameter $\kappa = 4$. Evidence shows that fluid viscosity enhancement leads to progressive shift of the current towards the inner walls of the bar. Simultaneously, the magnetic field

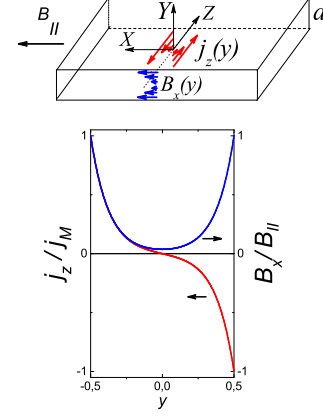


FIG. 7: Experimental setup (top panel) for thin sample placed in parallel field. Bottom panel: dimensionless current density j_z/j_M and azimuthal field B_x/B_0 profiles specified by Eqs.(35,34) for superconductivity at $\kappa = 4$ and $\nu_{cr} = 8$.

is pushed out from the sample bulk.

It is of particular interest the current density and (or) magnetic field profiles for superconductivity. Combining Eq.(19) and Eqs.(31) one obtains

$$j_z(y) = \bar{j} \cdot \kappa \frac{\cosh(\nu y)}{\cosh(\nu/2)}, \quad (32)$$

$$B_x(y) = -B_0 \frac{\sinh(\nu y)}{\sinh(\nu/2)}. \quad (33)$$

Note that Eq.(32) follows immediately from Navier-Stocks Eq.(7) when one puts $E_z = 0$. One may perform the integration of Eq.(32) using Maxwell equation $\text{rot} \mathbf{B} = \frac{4\pi}{c} \mathbf{j}$. In such a way we recover Eq.(33) and, moreover, confirm again the threshold condition $\kappa\beta = 1$.

Recall that the current (field) penetration length $\lambda = \sqrt{\eta\tau} = \frac{d_m}{2z(\Theta)}$ depends on the temperature. At high temperatures the fluid is non-viscous therefore the penetration length is small since $z \rightarrow \infty$. At low temperatures the penetration length increases. For bulky specimen at threshold temperature $T = T_c$ the penetration length is given $\lambda = \frac{d_m}{2}$. To confirm this finding, we put in Fig.6,b the exponential asymptote $B_x = B_0 \exp(-2\kappa(y + 1/2))$ imposed to magnetic field profile specified by Eq.(33).

It is of considerable interest the case of a specimen placed into external magnetic field B_{\parallel} parallel to the slab plane. Evidence shows that current distribution depicted in Fig.7 may prevent magnetic field penetration to the sample bulk. Again, for $E_z = 0$ the Navier-Stocks Eq.(7) allows one to find the current density profile

$$j_z(y) = -j_M \frac{\sinh(\nu y)}{\sinh(\nu/2)}. \quad (34)$$

After subsequent integration one obtains the magnetic field

distribution in the sample bulk

$$B_x(y) = B_{\parallel} \frac{\cosh(\nu y)}{\cosh(\nu/2)}. \quad (35)$$

where $B_{\parallel} = \frac{4\pi}{c} j_M \frac{d}{\nu} \tanh^{-1}(\nu/2)$. For actual geometry Eq.(13) reads $j_M = \frac{cB_{\parallel}}{2\pi d} \kappa$, therefore we obtain a modified threshold condition $\kappa\beta / \tanh^2(\nu/2) = 1$ for superconductivity. Intriguingly, for bulky sample $\nu \rightarrow \infty$ the latter coincides with threshold condition given by Eq.(19) for current carrying sample which confirm, in general, the Silsbee's²¹ hypothesis.

IV. TRANSITION FROM NORMAL STATE TO SUPERCONDUCTIVITY

A. Sample-size driven normal state to superconductivity transition

In Sec.III C we have demonstrated a possibility of the superconductivity phase for film thickness $d \geq d_m \kappa_m$. For thinner samples the resistivity remains finite. One expect that the shape of the temperature dependence of the resistivity would be sensitive to variation of the sample thickness. This effect is known in literature²²⁻²⁴ as so-called sample-size driven normal-to-superconductor state transition. Remarkably, our model predicts such a transition which has been shown in Fig.4 already. Indeed, for sample thickness changed from bigger $\kappa > 1$ to a smaller $\kappa < 1$ one, the shape of the resistivity curves $\rho(\nu)$ in Fig.4 changes drastically. Obviously, the temperature dependence of the resistivity duplicates this tendency since $\nu \sim 1/\sqrt{\eta} \sim T$. Actually, one would expect an abrupt change from "metallic" upturn $\frac{d\rho}{dT} > 0$ to "insulating" downturn $\frac{d\rho}{dT} < 0$ behavior as the sample size decreases. For $\kappa = 1$ the resistivity is constant given by Drude value $\rho = \rho_D$. Evidence shows that the experimental data for quench-condensed amorphous bismuth²³ reproduced in Fig.8a would be an example which supports our model predictions. We now intend to account for this effect. By the primary step, we found the correct thickness $d = 63.7\text{\AA}$ for certain sample instead of that $d = 74.27\text{\AA}$ ^{23,24} stated in Fig.8a.

Let us discuss first the properties of amorphous bismuth whose structure was analyzed in details in Ref.²⁵. It was confirmed that the molecular beam condensation of bismuth at helium temperature²⁶ results in the uniform filling of the substrate with atoms whose diffusion mobility is negligibly small. The film structure remains stable being characterized by a few weakly pronounced coordination spheres. Thicker layers $\geq 100\text{\AA}$ have a definitive structure with the first coordination sphere of radius $\sim 3.2\text{\AA}$ and 4-5 atoms included. Over the temperature range explored in Ref.²³ the layers of thicknesses, down to monatomic, exhibit the metallic conductivity. According to Ref.²⁵, the conductivity increases for less disordered layers of enhanced thickness. In view of immutable position of add-on Bi atoms on the film the carrier density is conventionally²⁵ believed to be a constant governed by valence electrons. However, the density of the conducting electrons was reliably measured²⁷ for only thick films $\geq 150\text{\AA}$,

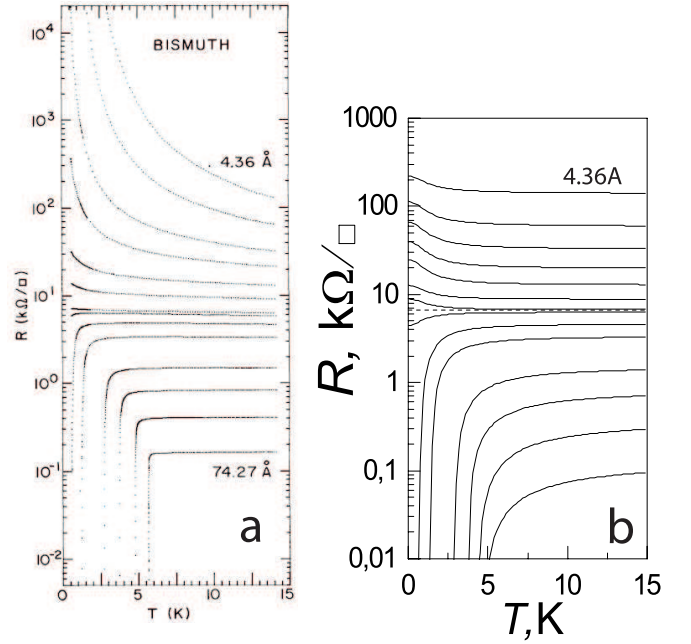


FIG. 8: Sheet resistance R_{\square} vs temperature for amorphous bismuth thin films: a) experimental data under Ref.²³ for sample thickness $d[\text{\AA}] = 63.7; 25; 14.8; 10.7; 7.9; 7.4; 6.7; 6.4; 6.2; 5.7; 5.4; 5.0; 4.65; 4.36$. b) calculated.

which is much greater than those explored in Ref.²³. We argue that conventional Hall measurements are highly desirable for reliable determination of carrier density.

We draw attention to the existence of a T-independent plane separatrix of the resistance data in Figure 8a. The latter corresponds to sample of thickness $d \simeq 6.5\text{\AA}$ and the sheet resistance $R_{\square} \simeq 6.5\text{k}\Omega$ counted for normal state at $T = 14\text{K}$. The separatrix matches the condition $\kappa = 1$ in our notations. Thus, we put $d_m = 6.5\text{\AA}$. Noticeably, the bulk resistivity $\rho_D = R_{\square} d_m = 420\mu\Omega\text{cm}$ is comparable to typical value $\sim 200\mu\Omega\text{cm}$ known from Ioffe-Regel²⁸ criteria $l \sim a$ for dirty metal, where a is the interatomic distance. Further, we will discuss the problem of transport in dirty metals. At a moment, we concentrate on the regular conductivity $\sigma = \rho^{-1}$ being, as usual, a measure of the disorder strength.

The careful analysis of the data in Fig.8a reveals the evidence of the superconductor transition at $T_{cr} = 0$ expected for sample of thickness $d \simeq 7.2\text{\AA}$ and the normal sheet resistance $R_{\square} \simeq 6\text{k}\Omega$ at $T = 14\text{K}$. The respective bulk resistivity yields $\rho_0 = R_{\square} d = 410\mu\Omega\text{cm}$ at $T = 14\text{K}$. This result is of extreme interest since it allows to deduce the key parameters of our model. Indeed, one may find the reduced sample size $\kappa_m = d/d_m = 1.12$ and, in turn, parameter $z_{m0} = 0.54$ from the critical plot in Fig.5a.

Recall that for bulky amorphous bismuth the critical temperature is known $T_c = 6.1\text{K}$. Noticeably, at elevated temperatures the all resistance curves below separatrix in Fig.8a demonstrate a flat behavior indicating the predominant role of structure assisted disorder²⁵. For each curve below the separatrix we use the data²³ to extract the critical temperature

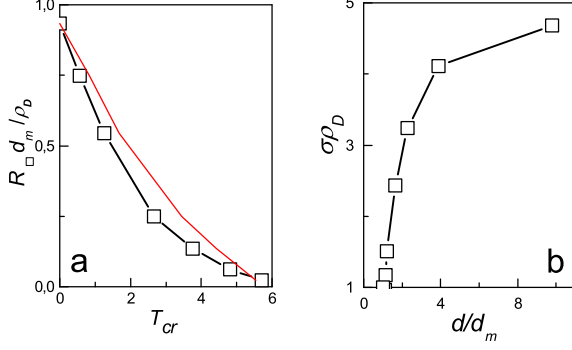


FIG. 9: a.Reduced sheet resistance $R_{\square} d_m / \rho_D$ at $T = 14\text{K}$ vs critical temperature of superconductivity T_{cr} . Theoretical result is shown by the red curve. b.Dimensionless conductivity $\sigma \rho_D$ vs reduced sample thickness $\kappa = d/d_m$. The values ρ_D, d_m correspond to separatrix curve in Fig.8a.

$T_{cr} < T_c$, reduced layer thickness κ and, then the transport coefficients: $R_{\square}, \rho = R_{\square} d, \sigma = 1/\rho$ at $T = 14\text{K}$. Following the standard practice, we plot in Fig.9a the sheet resistance vs critical temperature $R_{\square}(T_{cr})$. Moreover, we plot the dependence of conductivity vs sample thickness $\sigma(\kappa)$ in Fig.9b. As in Ref.²⁵ the disorder becomes stronger in thinner films. Combining the dependencies $R_{\square}(T_{cr})$ and $\sigma(\kappa)$ we obtain the temperature threshold either in terms of reduced size $T_{cr}(\kappa)$ or conductivity $T_{cr}(\sigma)$. Both dependencies are illustrated in Fig.10. We first focus on the critical diagram $T_{cr}(\kappa)$ which resembles theoretical one found above within constant mobility scenario(see Fig.5c). In contrast to our model, both the thickness and the film conductivity(mobility) vary in the experiment. To account for both changes we use Eqs.(21),(24) and the condition $z_{cr}(\kappa) = z(\xi)$ valid for arbitrary film thickness. Finally, we obtain threshold temperature for arbitrary sample size and disorder as it follows

$$T_{cr} = T_F \left[\left(\frac{z_{cr}^2(\kappa)}{z_{m0}^2} \sigma(\kappa) \rho_0 - 1 \right) \frac{1}{\gamma} \right]^{1/2}, \quad (36)$$

where z_{m0}, ρ_0 are constants deduced above for superconductor transition at $T_{cr} = 0$. Note that the previous result for bulky sample specified by Eq.(28) follows from Eq.(36) when $\kappa \rightarrow \infty$ and, then $z_{cr}(\kappa) = 1$ and $\sigma \rho_0 / z_{m0}^2 = \mu / \mu_{\min}$.

With the help of Eq.(36) we are able to fit the experimental dependence $T_{cr}(\kappa)$ represented in Fig.10a. We use the dependence $\sigma(\kappa)$ in Fig.9b and Eq.(36) keeping γ/T_F^2 as a fitting parameter. Our best fit shown by the red curve Fig.10a yields a parameter $\gamma/T_F^2 = 0.5\text{K}^{-2}$. This finding help us to write down the bismuth relaxation length as it follows

$$l_0/l_{\eta} = 1 + 0.5 \cdot T^2 \quad (37)$$

valid for temperature range $T < T_c$. The dependence specified by Eq.(37) is extrapolated up to high temperatures $T \leq 14\text{K}$ and, then plotted in Fig.11.

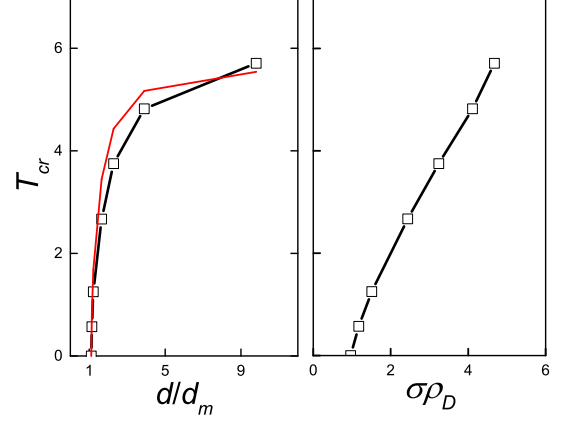


FIG. 10: Critical temperature T_{cr} deduced from Fig.8a vs: a) sample size $\kappa = d/d_m$ and b) reduced conductivity $\sigma \rho_D$. The red curve shows the best fit with the help of Eq.(36).

To illustrate the robustness of our approach, we compare the experimental dependence $R_{\square}(T_{cr})$ in Fig.9a with that visualized by the red curve and followed from combined use of Eq.(36), dependence $\sigma(\kappa)$ and newly extracted parameter γ . The theory predictions are close to experimental data.

Let us now reproduce films resistance data set²³ plotted in Fig.8b. Combining Eqs.(24),(18),(37) along with the relationships $\nu = 2\kappa z(\xi), z_m = \frac{z_{m0}}{\sigma(\kappa)\rho_0}$ we obtain the sheet resistance for certain layer thickness. In contrast to bottom curves related to thick films, the actual sample thicknesses for curves above the separatrix were not indicated in Ref.²³. To fix the situation, we compare the experimental value of the resistance R_{\square} at 14K for each film $d < d_m$ with that followed from our calculations and, then estimate the layer thickness roughly. The result of our efforts is shown in Fig.8b. As expected, the change from downturn $\frac{d\rho}{dT} > 0$ to upturn $\frac{d\rho}{dT} < 0$ behavior occurs when $\kappa = 1$. Actually, the "insulating" behavior of the resistance for thin $\kappa < 1$ samples follows from relationship $\frac{d\rho}{dT} \sim \frac{d\eta}{dT} \sim \frac{d\tau_{\eta}}{dT} < 0$. The sets in both panels of Fig.8 resemble one another excepting the shape and magnitude of the "insulating" curves above the separatrix. We attribute this discrepancy to possible hopping transport which would be relevant for Bi film of atomic length scale²⁹.

It is instructive to estimate the Bi-samples parameters. We remind you that there was no study of carrier density in Ref.²³. In view of typical sample resistivity $\rho_0 = 410\mu\Omega\text{cm}$ close to that given by Ioffe-Regel formalism²⁸ for dirty metal, we use this theory³⁰ to calculate the carrier mean free path l . For a sample of size $d = 7.2$ argued above to be a superconductor at $T_{cr} = 0$ we obtain $l = \frac{e^2 Z^{2/3}}{3\hbar} \rho_0 = 9.9\text{\AA}$, where $Z = 5$ is the number of valence electrons for bismuth. The present model gives the length of viscosity relaxation $l_0 = \frac{5d_m^2}{4z_{m0}^2 l} = 18\text{\AA}$ at $T = 0$. While $l < l_0$, both lengths demonstrate the same order of magnitude¹³ and, hence support the applicability of

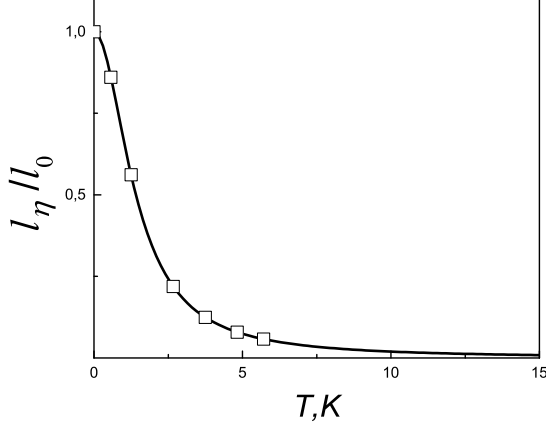


FIG. 11: Dimensionless e-e relaxation time for amorphous bismuth vs temperature ($l_0 = 18\text{\AA}$) extracted from experimental data²³. Square dots visualize the data in Fig.8 associated with superconductor transition at $T < T_c$.

the hydrodynamic approach in question.

B. Phase diagram of superconductivity B(T) for massive specimen

The all previous discussion concerned the zero-current mode of the galvanic measurements. We demonstrated that growth of temperature and(or) drop of the sample size destroys the superconductivity. In general, the enhancement of the applied currents and(or) magnetic fields is known^{19,20,31} to break down the superconductivity as well. Noticeably, the typical scale of critical magnetic fields ($\leq kG$) corresponds to classical limit $\Omega_c\tau \ll 1$ regarding the carrier transport. We now examine the influence of finite current and(or) magnetic field on the superconductivity.

Our previous findings confirmed the crucial role of diamagnetic currents regarding the origin of superconductivity. Usually, the diamagnetic currents are generally believed to be caused by cyclotron movement of electrons whose orbits are closed to (but contactless) the inner sample walls. Noticeably, one must distinguish the diamagnetic contribution to susceptibility with paramagnetic one caused by electron reflections from the sample walls, i.e so-called skipping trajectories.

Within classical range of the magnetic fields $\Omega_c\tau \ll 1$ one may imagine an electron moved along the cyclotron orbit during the mean free time and, then experienced a collision with phonons and(or) impurities. Importantly, the curvature of cyclotron orbit trajectory counted for subsequent collisions increases with magnetic field. For cyclotron trajectories of an electron in the vicinity of the top(bottom) sample wall(see Fig.1) one must account for only the local magnetic field, namely B_0 in our notations. Evidence shows that the thickness of the layer filled by diamagnetic current flux could be a linear function of transverse magnetic field, i.e. $\delta(1 + bB_0)$.

Here, we write down a phenomenological constant b . Finally, we introduce a modified sample-size parameter

$$\kappa(B_0) = \frac{\kappa}{1 + bB_0}, \quad (38)$$

which depends on the transverse magnetic field B_0 . The superconductivity threshold transition criteria given by Eq.(19) now yields

$$\kappa(B_0)\beta(\nu) = 1. \quad (39)$$

For the most important case of the massive specimen $\kappa \rightarrow \infty$, we find $\beta(2z\kappa) \simeq 1/z\kappa$. Using Eq.(29) one obtains phase diagram of superconductivity

$$B_0 = B_c \frac{(1 + (z_m^{-2} - 1)\Theta^2)^{-1/2} - z_m}{1 - z_m} \quad (40)$$

where $B_c = (z_m^{-1} - 1)/b$ is the critical magnetic field at zero temperature. As an example, the magnetic field driven phase diagram specified by Eq.(40) for fixed $z_m = 0.8$ is plotted in Fig.12b. For $z_m \leq 1$ the phase diagram given by Eq.(40) can be fitted by quadratic dependence

$$B_0 = B_c(1 - \Theta^2) \quad (41)$$

usually reported to be a good approximation for the most of elementary superconductors. Note that in the vicinity of critical temperature $T_c - T \ll T_c$ Eq.(40) gives a linear slope $|\frac{1}{B_c} \frac{dB_0}{d\Theta}| = (1 + z_m)z_m \leq 2$ close to that $|\frac{1}{B_c} \frac{dB_0}{d\Theta}| = 2$ provided by Eq.(41). This result is confirmed by numerous experiments. Using Eq.(28) one may find out the critical magnetic field at zero temperature

$$B_c = b^{-1} \left(\sqrt{1 + \gamma(T_c/T_F)^2} - 1 \right) \quad (42)$$

for massive samples. At low temperatures $\sqrt{\gamma}T_c/T_F \ll 1$ the critical temperature obeys quadratic dependence $B_c \sim \frac{\gamma}{2b} \left(\frac{T_c}{T_F} \right)^2$ while becomes linear in the opposite high temperature case, i.e. $B_c \sim \frac{\sqrt{\gamma}}{b} \frac{T_c}{T_F}$.

We emphasize that for arbitrary sample size Eq.(39) defines the threshold surface in $T - d - B$ space. The latter can be readily represented in terms of dimensionless sample size κ , then the critical temperature Θ_{cr} and magnetic field B_0/B_c related to massive specimen values. The 3D plot is shown in Fig.(12)a for fixed $z_m = 0.8$ and finite sample size $\kappa < 3$. As expected, for massive sample, i.e. when $\kappa \rightarrow \infty$ the critical diagram $B_0(T)$ approaches that depicted in Fig.(12)a.

C. Magnetic field turned the normal phase to superconductivity transition

Recall that the result of Sec.IV A concerned the change from upturn $\frac{d\rho}{dT} > 0$ to downturn $\frac{d\rho}{dT} < 0$ behavior of the sheet resistance as the sample thickness decreased. At low currents this happens for certain sample size when $\kappa = 1$. Obviously, the current enhancement leads to subsequent growth

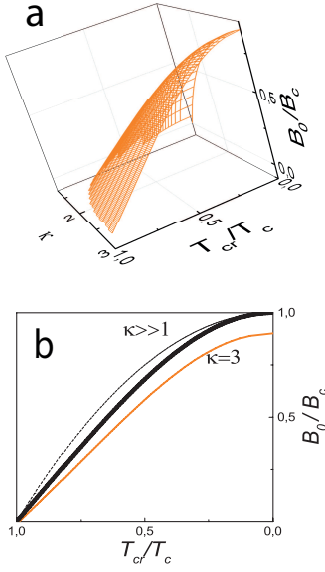


FIG. 12: a) 3D plot of critical surface given by Eq.(39) b) Phase diagram of superconductivity given by Eq.(40) for $z_m = 0.8$ for massive ($\kappa = \infty$) and finite size sample $\kappa = 3$. The dashed curve depicts the empirical dependence specified by Eq.(41).

of the transverse magnetic field (see Fig.6a). Remind that the strength of diamagnetic currents at the upper(down) sample walls is linear to local transverse field B_0 . Hence, the derivative $\frac{d\rho}{dT}$ would change the sign when $\kappa = 1 + bB_0$. We conclude that for fixed slab thickness the enhanced current could result in the resistance behavior similar to that seen in Fig.8a. By now, we unaware of any experiment dealing with the proposed effect. In contrast, a film placed into perpendicular magnetic field B_\perp demonstrates the magnetic field driven change of sheet resistance shape^{32–34}. The experimental setup is shown in Fig.13b,inset. The typical resistance set measured for different fields is reproduced in Fig.13a under Ref.³³. We now intend to examine this effect.

We argue that the applied perpendicular field B_\perp produces the tangential component of the magnetic field $B_y \parallel B_\perp$ at the sample side faces shown by grey color in Fig.13b, inset. Indeed, let us assume the sample as a thin disk which, in turn, can be viewed as limiting case of the rotation ellipsoid. In this case the search of the induced magnetic field yields the textbook³⁵ result $B_y = \frac{B_\perp}{1-N}$, where $0 < N < 1$ is so-called demagnetization factor. For thin disk $N \simeq 1$. Recall that whenever the tangential component of the magnetic field is present at arbitrary sample surface the superconductivity becomes suppressed. We speculate that the component B_y present at the grey face of the film side plays the role of magnetic field B_0 embedded into Eq.(38). As a result, we obtain the modified criteria

$$\kappa = 1 + b^* B_\perp. \quad (43)$$

for derivative $\frac{d\rho}{dT}$ change instead of previous one $\kappa = 1$ valid in absence of the perpendicular magnetic field. Here

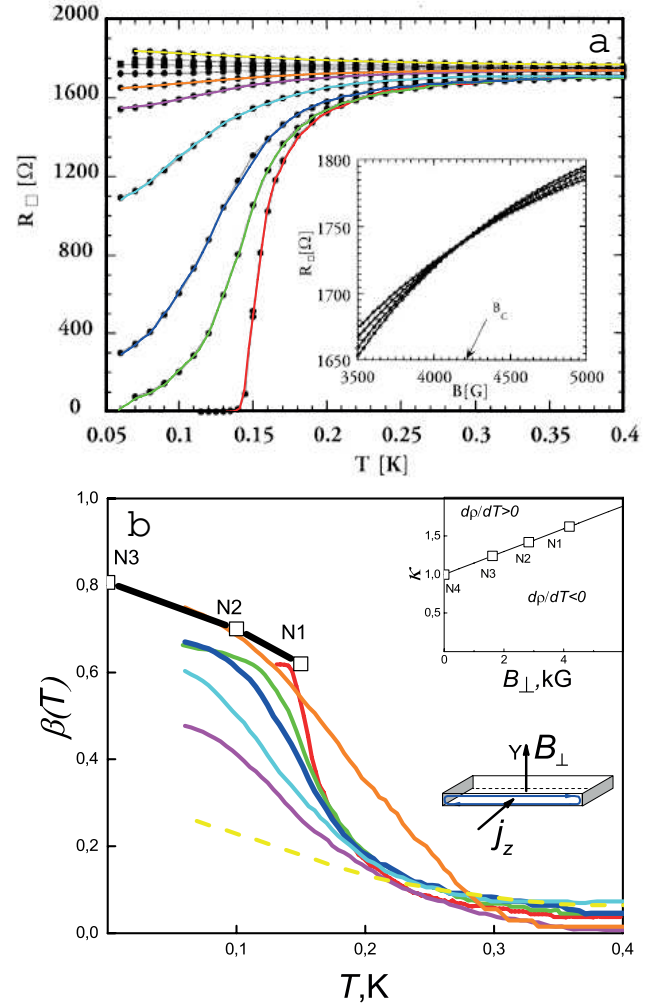


FIG. 13: a) Sheet resistance for Mo_{21}Ge sample N1 ($d = 80 \text{ \AA}$) under Ref.³³ for $B_\perp = 0, 0.5; 1; 2; 3; 4; 4.4; 4.5; 5.5; 6 \text{ kG}$. (from bottom to top) b) Universal function β vs temperature deduced from each of the colored curves in panel a. Inset: (top) dependence specified by Eq.(43); (bottom) Experimental setup³³. Black squares represent the data for samples denoted in Table I.

$b^* = b/(1 - N)$ is the sample dependent coefficient. The linear dependence specified by Eq.(43) is reproduced in Fig.13b,inset. Remarkably, a similar dependence was reported in experiment³⁴.

We argue that separatrix of the sheet resistance curves in Fig.13a occurs for sample N1 of thickness $d = 80 \text{ \AA}$, the sheet resistivity $R_{cr} = 1750 \Omega$ in presence of magnetic field $B_\perp = 4.19 \text{ kG}$. Then, at zero field the resistance data demonstrate the superconductor transition at $T_{cr} = 0.15 \text{ K}$. Similar studies³³ reported for thinner ($d = 70 \text{ \AA}$) sample N2 give the respective values collected in Table I. For both samples the normal resistivity is the same, namely $\rho = 1400 \mu\Omega\text{cm}$ at $T = 0.14 \text{ K}$, indicating a similar disorder in both cases. Therefore, we use the basic results of our model implying a constant disorder strength. Using the parameters of samples N1,2 and Eq.(43) we define the minimal size value $d_m = 50 \text{ \AA}$ and co-

TABLE I: Parameters of the Mo₂₁Ge samples N1,2 studied in Ref.³³ and predicted(N3,4) by present theory.

Samp.	d [Å]	κ	B_{\perp} [kG]	R_{cr} [Ω]	T_{cr} [K]	$z(T_{cr})$	$\beta(T_{cr})$
N1	80	1.62	4.19	1750	0.15	0.89	0.62
N2	70	1.42	2.82	2026	0.1	0.83	0.70
N3	61	1.24	1.62	-	0	0.70	0.81
N4	50	1	0	-	-	0	-

efficient $b^* = 1.48 \cdot 10^{-4} \text{G}^{-1}$. We calculate the reduced size $\kappa = d/d_m$ for each sample and, then use the critical diagram in Fig.5a to find out parameter z and value of the function $\beta(2\kappa z)$ respectively. The results are archived in Table I.

Further analysis of the resistance data for sample N1 in Fig.13a gives evidence of superconductor transition at $T_{cr} = 0$ which would occur at a certain magnetic field $B_{\perp} \simeq 1.1 \text{kG}$. This case of the special interest providing disclosure of key parameter z_m of our model. Indeed, for reduced film size $\kappa = 1.62$ of sample N1 the solution of Eqs.(39),(38) under the substitution $bB_0 \rightarrow b^*B_{\perp}$ yields the parameter $z = z_m = 0.7$. Then, we find $\kappa_m = 1.24$ with the help of critical diagram shown in Fig.(5)a. We conclude that superconductivity transition at $T_{cr} = 0$ and zero magnetic field would be feasible for hypothetical sample of thickness $\kappa_m d_m = 61 \text{Å}$ labeled as N3 in TableI. According to Eq.(38) the sample N3 would exhibit a change in metallic vs "isolating" behavior of resistance at $B_{\perp} = 1.62 \text{kG}$. Also, we collect in TableI the parameters for even thinner hypothetic sample N4 of thickness $d = d_m = 50 \text{Å}$ which would exhibit a constant resistance $\rho = \rho_D$ at zero magnetic field(see Fig.11b, inset).

Recall that resistivity specified by Eq.(18) depends on the universal function $\beta(T)$. For each curve in Fig.13a the function $\beta(T)$ can be extracted. One take an interest whether the

all curves can be scaled by the same dependence $\beta(T)$. Taking into account the modified parameter specified by Eq.(38) and Eq.(18) we calculate and, then plot in Fig.13b the result. In contrast to rough resistance data ranges from zero to values of the order of $\sim k\Omega$, the range of function $\beta(T)$ magnitude falls into much narrow range $0.3 < \beta(T) < 0.8$ seen in Fig.13b. For completeness, we add in the same plot the dependence $\beta(T_{cr})$ followed from TableI for samples N1-3 when the magnetic field is zero. In conclusion, the present analysis of the experimental data³³ provides strong support in favor of our model.

V. CONCLUSIONS

In conclusion, we discover the self-consistent Hall Effect in a bar conductor taking into account both the diamagnetism and finite viscosity of 3D electron liquid. We demonstrate that under certain condition the resistivity of the sample vanishes exhibiting the transition to superconductivity. The current is pinched nearby the inner sample walls while the magnetic is pushed out from the sample bulk. Within low current limit the threshold temperature of superconductivity is calculated for arbitrary carrier dissipation and the sample size. For sample size and(or) carrier mobility being lower than a certain minimum values the superconductivity state cannot be realized. Sample-size and magnetic field driven transition from zero-resistance state to normal state is compared with experimental data. Phase diagram in terms of threshold temperature vs applied current and(or) magnetic field is calculated. The temperature dependence of the e-e scattering time for amorphous bismuth is extracted from the experimental data for the first time.

¹ E.H. Hall, American Journal of Mathematics, **2**, 287 (1879).

² A.I. Anselm, Vvedenie v fiziku poluprovodnikov(in Russian), Nauka, Moscow, (1978).

³ M.A. Matzek and B.R. Russell, Am.J.Phys. **36**, 905 (1968).

⁴ Kirk T. McDonald, <http://www.physics.princeton.edu/mcdonald/examples/wire.pdf>

⁵ M.S. Steinberg, Phys.Rev. **109**, 1486 (1958).

⁶ R.N. Gurzhi, Sov.Phys.JETP, **17**, 521 (1963).

⁷ M. Dyakonov and M. Shur, Phys.Rev.Lett. **71**, 2465 (1993).

⁸ L.D. Landau, Z. Phys., **64**, 629 (1930).

⁹ D.V. Sivukhin, A Course of General Physics, vol. III, Electricity(in Russian), Nauka, Moscow, (1996).

¹⁰ A.A. Vlasov, Makroskopicheskaya Elektrodynamika, Moscow, Fizmatlit, (2005).

¹¹ Q. Shi et al, Phys.Rev.B, **89**, 201301(R) (2014).

¹² P.S. Alekseev, Phys.Rev.Lett. **117**, 166601 (2016).

¹³ M.V. Cheremisin, arXiv:2109.14005

¹⁴ H. Kamerlingh Onnes, Communication from the Physical Laboratory of the University of Leiden, 122b, 124c (1911); 133a, 133c (1913).

¹⁵ W. Meissner, Ann. Physik (5) **13**, 641 (1932).

¹⁶ L. Landau and I. Pomerantschuk, Phys. Z. Sovietunion **10**, 649

(1936).

¹⁷ J.J. Quinn and R.A. Ferrell, Phys. Rev. **112**, 812 (1958).

¹⁸ A.A. Abrikosov and I. M. Khalatnikov, Rep.Prog.Phys.**22**, 329 (1959).

¹⁹ W. Meissner, Physics-Uspekhi **13**, 639 (1933).

²⁰ W. Meissner, R.Ochsenfeld, Naturwissenschaften **21**, 787 (1933).

²¹ F.B. Silsbee, Journal of the Washington Academy of Sciences **6**, 79 (1916).

²² H.M. Jaeger, D.B. Haviland, B.G. Orr, and A.M. Goldman, Phys. Rev. B **40**, 182 (1989).

²³ D.B. Haviland, Y.Liu and A.M.Goldman, Phys.Rev.Lett. **62**, 2180 (1989).

²⁴ Y. Liu et al, Phys.Rev.B **47**, 5931 (1993).

²⁵ Yu.F. Komnik, B.I. Belevtsev and L.A. Yatsuk, Sov. Phys. JETP **36**, 1177 (1973).

²⁶ W. Buckel and R. Hilsch, Zs. Phys. **138**, 109 (1954).

²⁷ O. Hunderi, J. Phys.F: Metal Phys. **5**, 2214 (1975).

²⁸ A.F. Ioffe and A.R. Regel, Prog. Semicond. **4**, 237 (1960).

²⁹ B.I. Belevtsev, Yu.F. Komnik and A.V. Fomin, Fizika Tverdogo Tela **30**, 2773 (1988).

³⁰ M. Gurvitch, Phys. Rev. B, **24**, 7404 (1981).

³¹ F.B. Silsbee, J.Franklin Inst. **184**, 111 (1917).

- ³² A.F. Hebard and M.A. Paalanen, Phys.Rev.Lett. **65**, 927 (1990);
M.A. Paalanen, A.F. Hebard and R.R. Ruel, *ibid* **69**, 1604 (1992).
- ³³ Ali Yazdani and Aharon Kapitulnik, Phys.Rev.Lett. **74**, 3037 (1995).
- ³⁴ N. Markovic, C. Christiansen, and A.M. Goldman Phys.Rev.Lett. **87**, 5217 (1998).
- ³⁵ A.C. Rose-Innes and E.H. Rhoderick, Introduction to Superconductivity, Pergamon Press, New York, (1978).